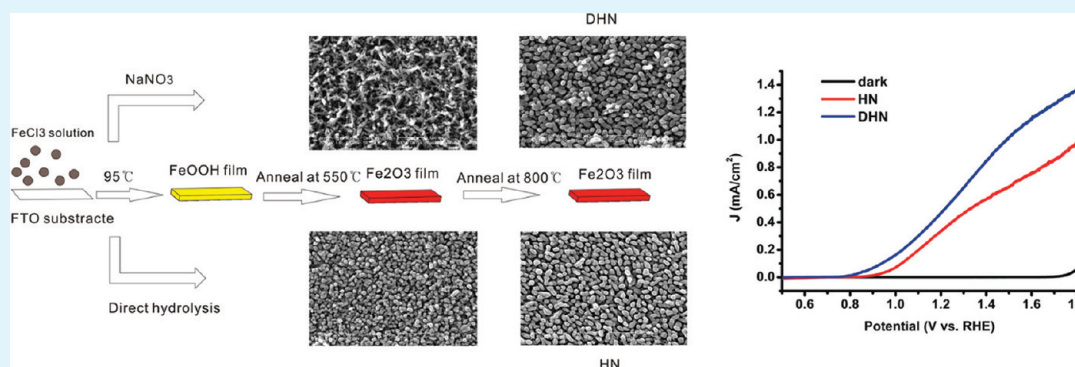# Lattice Defect-Enhanced Hydrogen Production in Nanostructured Hematite-Based Photoelectrochemical Device

Peng Wang, Degao Wang, Jun Lin, Xiaolong Li, Cheng Peng,* Xingyu Gao, Qing Huang, Jianqiang Wang, Hongjie Xu, and Chunhai Fan*

Shanghai Institute of Applied Physics, Chinese Academy of Sciences, Shanghai 201800, China

ABSTRACT: Nanostructured hematite photoanodes have been intensively studied in photoelectrochemical (PEC) water splitting for sustainable hydrogen production. Whereas many previous efforts have been focused on doping elements in nanostructured hematite (α-Fe$_2$O$_3$), we herein demonstrated an alternative approach to enhance the PEC performance by exploiting intrinsic nanostructuring properties of hematite. We found that the introduction of lattice defects effectively decreased the flatband potential and increased the charge transport mobility of nanostructured hematite, hence enhance the light harvest for more efficient hydrogen production via PEC. The nanostructured hematite photoanodes with lattice defects yielded water-splitting photocurrent density of 1.2 mA/cm^2 at 1.6 V vs reversible hydrogen electrode (RHE), which excelled defect-free ones by approximately 1.5 folds. This study thus provides a new strategy for finely tuning properties of nanostructured hematite photoanodes and enhancing the water-splitting ability of PEC.

KEYWORDS: nanostructured hematite, lattice defect, water splitting, photoelectrochemical, hydrogen, light harvest

INTRODUCTION

It is urgent to develop clean and renewable energy in order to address the two critical issues of energy depletion and environmental pollutions.[1−3] Hydrogen energy, as a carbon-free and high-efficiency secondary energy, has been widely regarded as an ideal way to the solution of energy and environment problems.[4−7] As the carrier of hydrogen energy, hydrogen production from water-splitting using primary energy sources such as solar energy,[8−10] electricity,[11] or thermal energy[12,13] has been a major concern. Among many routes to splitting water under solar light, photoelectrochemical (PEC)-based water-splitting represents a very promising strategy for high-efficiency, cost-effective and environmentally benign hydrogen production.[6,7] Since the pioneering work of using TiO$_2$ as the photoanode material for PEC water-splitting,[149] various metal oxide materials, e.g.. Fe$_2$O$_3$,[10,15−18] WO$_3$,[19−23] ZnO,[24−27] KNbO$_3$[28] have been actively explored for water splitting. Hematite (α-Fe$_2$O$_3$) has received considerable attention as a promising photoanode material. Hematite is the abundant mineral with excellent chemical stability on earth, with favorable band gap of 1.9−2.2 eV[6] for solar harvesting that allows to absorb up to 40% portion of the solar radiation. It also has a suitable energy position of the valence band edge for oxygen evolution in water oxidization. However, the photo-response of hematite suffers from short hole-diffusion length (2−4 nm)[29,30] and poor charge transport (1×10^{-2} to 1×10^{-1} cm^2 V^{-1} s^{-1})[31] that largely limits its practical applications.

More recently, many hematite nanostructures have been developed to circumvent the problem of short diffusion length of photogenerated holes. These include hematite nano-particles,[32] nanotubes,[33] and nanorods[34−36] with sizes comparable to the hole-diffusion length scale, which were employed to reduce the electron−hole recombination losses in PEC water splitting. In addition, these nanostructured hematite can increase the light absorption coefficient and the band gap energy while reduce the carrier-scattering rate due to their large surface area and size-dependent properties, which are also beneficial for photolysis of water. On the other hand, hematite nanostructures are often doped with various elements such as Ti,[37−40] Si,[38,39,41] Zn,[39,40] Al,[40,42] Cr,[43] Mg,[44] Sn,[37,44,45] Pt,[46]

ACS Publications © 2012 American Chemical Society

2295

dx.doi.org/10.1021/am300395p | ACS Appl. Mater. Interfaces 2012, 4, 2295−2302

and Au[47] to increase the mobility of charge transport. For example, Ti dopants served as electron donors that enhanced electrical conductivity of hematite via the polaron hopping mechanism,[37,40] and Sn dopants enhanced the optical absorption coefficient via distortion of the hematite lattice and also served as electron donors to increase the carrier density of hematite nanostructures.[30] Very recently, Goncalves et al. developed a high-efficiency PEC with pure mesoporous hematite photoanodes and reached a high photocurrent of 1.1 mA/cm^2 at 1.23 V vs reversible hydrogen electrode (RHE).[48] It is expected that the water-splitting efficiency can be further increased by finely tuning the nanostructure, grain boundaries and crystallographic orientation. Hence, we herein focus on studying the effect of lattice defects in hematite nanostructures on the PEC water splitting efficiency.

■ EXPERIMENTAL SECTIONS

Materials. Fluorine-doped tin oxide coated glasses (FTO, TEC-15) were purchased from NGS glass and copper foil conductive tape (tape 1182) was obtained from 3 M United Kingdom PLC Electrical Products Group. Ferric chloride (FeCl$_3$·6H$_2$O), NaNO$_3$ and acetone, anhydrous ethanol were all A.R. grade and purchased from Sinopharm Chemical Reagent Co. Ltd. at Shanghai. All aqueous solutions were prepared with deionized (DI) water from Milli-Q-Water (Millipore Corp, 18.2 MΩ cm at 298 K).

Methods. Hematite films were prepared on a fluorine-doped tin Oxide (FTO) glass substrate with a modified procedure described in the literature.[49] In detail, A Teflon-lined stainless steel autoclave was filled with 20 mL aqueous solution, which containing 0.1 M of FeCl$_3$·6H$_2$O and 1.0 M NaNO$_3$. A piece of FTO glass was cleaned ultrasonically in pure water, ethanol, and acetone and then rinsed in water again before chemical bath deposition. Then the FTO glass was put into the autoclave and heated at 95 °C. A uniform yellow layer of iron oxyhydrodides (FeOOH) film was formed on the FTO substrate
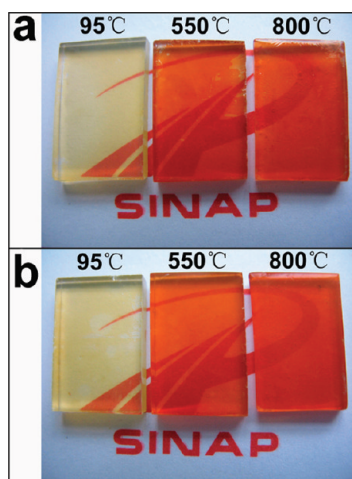

Figure 1. Digital images of electrodes obtained from experiment. The electrodes obtained in the absence and in the presence of NaNO$_3$ are shown in panels a and b, respectively. Each panel shows the electrodes synthesized at 95, 550, and 800 °C, respectively.

after 6 h (see Figure 1a, b). The FeOOH-coated FTO substrate was then washed with water more than 3 times to remove all the inorganic salts and subsequently annealed in air in a box furnace. The temperature of furnace was rising (the rate of temperature rise was 40 °C per minute) from room temperature to the set point of 550 °C and then maintained 2 h for completing the conversion from FeOOH to nanostructured hematite. After further annealing of 10 min at 800 °C, the as-prepared hematite-nanostructured photoanodes were

cooled slowly to room temperature for PEC measurements. In a different approach, hematite-nanostructured photoanodes were prepared with the same conditions except the lack of using inorganic salt NaNO$_3$ in the electrolyte during the process of chemical bath deposition.

Characterization. The XRD experiments of hematite-nanostructured photoanodes was performed under the theta-2theta scan mode at BL14B1 beamline of Shanghai Synchrotron Radiation Facility (SSRF) with bending magnet light source. In detail, the sample was put at the center of Huber 5021 diffractometer, moreover, in order to distinguish the possible adjacent diffraction peak, scan step is set as 0.02 degree with incident X-ray energy 10K eV of wavelength 1.2398 Å. The morphologies of samples were characterized by Scanning Electron Microscope (SEM, JME2011, JEOL, Japan). UV−Vis absorption spectra were collected by Hitachi U-3010 spectrophotometer (Hitachi Co. Ltd., Japan). Mössbauer spectra were measured using a constant acceleration transmission mode with a 57 Co/Rh source at room temperature. The velocity was calibrated with a 25 μm α-Fe foil, and the Isomer Shift (IS) was relative to the center of α-Fe at room temperature. The spectra were fitted with the software of Moss Winn.[50]

PEC Measurements. Hematite-nanostructured photoanodes with a bare portion of FTO substrate was bonded with a copper wire and then sealed on all edges with epoxy resin except a bare area of 0.5 cm^2 for photo excitation. All photoelectrochemical measurements were tested in a three electrode configuration with the Pt counter electrode, the Ag/AgCl reference electrode and the working electrode of hematite-nanostructured photoanode. An aqueous solution of 1.0 M NaOH (pH 13.6) after deaerating with a nitrogen flow was filled in a quartz PEC cell and used as the electrolyte. A xenon lamp (300 W, Perfect Light Corp. Ltd. Beijing) with an infrared filter (absorbance ≥780 nm) was applied as the illumination source and directly radiated on the quartz photoelectrochemical cell. The radiation intensity at working electrode was measured as 100 mW/cm^2 by a solar power meter (TES-1333, ZhongXuan Electronic Corp. Ltd. Shanghai). In a typical experiment, a sample with 0.5 cm^2 area of photoresponse surface was immersed in electrolyte in PEC cell and illuminated under the artificial simulated sunlight initiated from the infrared filtered xenon lamp, and the incident photon-to-current conversion efficiency (IPCE) spectra were collected by CHI 660D (Chenhua Corp. Ld., Shanghai) and the IPCE data could be obtained with the following equation[7]

$$IPCE = \frac{1240I}{P\lambda}100\% \tag{1}$$

where I was the photocurrent density (mA/cm^2), P (mW/cm^2), and λ (nm) was the intensity and wavelength of the incident light. The Electrochemical AC impedance spectroscopy were performed both in the dark condition and in the bright condition in a three electrode configuration system in 1.0 M NaOH solution with a sinusoidal perturbation with 5 mV amplitude and frequencies ranging from 100 kHz to 1 Hz. Capacitance values were derived from the impedance-potential curves obtained at each potential with frequency of 1 kHz in the dark condition and Mott−Schottky plots were generated from the capacitance values. The collected potentials vs Ag/AgCl were converted to the reversible hydrogen electrode (RHE) scale according to the Nernst equation[45,51]

$$E_{RHE} = E_{Ag/AgCl} + 0.059pH + E^o_{Ag/AgCl} \tag{2}$$

where E_{RHE} was the converted potential vs RHE, $E^o_{Ag/AgCl}$ was 0.1976 V at 25 °C, and $E_{Ag/AgCl}$ was the experimental potential against the Ag/AgCl reference. Since the solution pH was 13.6, the $E_{Ag/AgCl}$ could be converted to E_{RHE} according to the following equation

$$E_{RHE} = E_{Ag/AgCl} + 1 \tag{3}$$

■ RESULTS AND DISCUSSION

The hematite nanostructured photoanodes were prepared both in the presence and in the absence of NaNO$_3$ during the
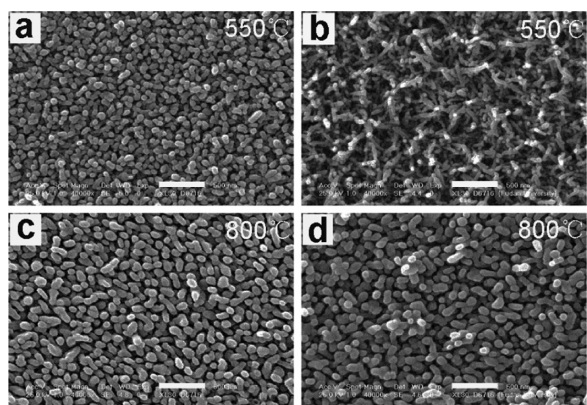
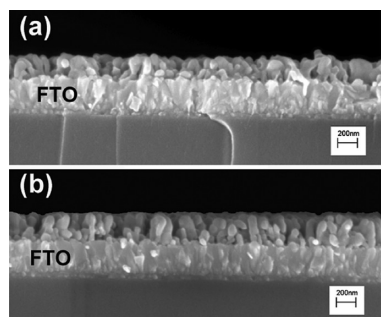**Figure 2.** SEM images of (a, c) HN and (b, d) DHN sintered at 550 and 800 °C. Scale bars represent 500 nm.

Figure 3. Cross-sectional SEM images collected fo (a)r HN and (b) DHN. All scale bars are 200 nm.
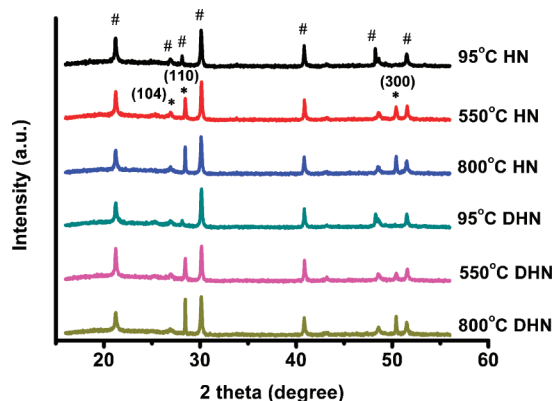

Figure 4. XRD spectra ($\lambda = 1.2398$ Å) of HN and DHN sintered at 95, 550, and 800 °C. The diffraction peaks of hematite and SnO_2 are indicated by * and #, respectively. The SnO_2 diffraction peaks originated from the FTO substrate.

chemical bath deposition step. Therefore, two kinds of hematite-nanostructured films were obtained: one was none of lattice defects in hematite nanostructures (namely HN) and the other was within lattice defects in hematite nanostructure (namely DHN). The presence of inorganic salt may produce many lattice defects in nanocrystalline, and the lattice defects could not be totally removed after two steps of annealing for conversion from FeOOH to hematite-nanostructured. The morphologies of the as-prepared HN and DHN photoanodes were first investigated by Scanning electron microscopy (SEM). From appearance (see Figure 1), no differences were observed between HN photoanode and DHN photoanode at 95 °C, 550

and 800 °C respectively. However at 550 °C, the SEM images in Figure 2 revealed that the diameter of hematite nanomaterial on DHN was about 30 nm (figure 2b), narrower than the diameter 60 nm of HN's (Figure 2a), and the length in DHN is longer than HN's. Obviously, the diameter and length differences between DHN and HN were both caused by adding inorganic salt $NaNO_3$ during chemical bath deposition in photoanode preparation. After annealing at 800 °C, DHN and HN became similar diameter of about 120 nm (Figure 2c, d), and similar thickness of about 200 nm of photoresponse hematite layer (Figure 3).

The structure information of HNP-D and HNP photoanodes were collected by X-ray powder diffraction (XRD) at the beamline BL14B1 of Shanghai Synchrotron Radiation Facility (SSRF). According to the reference pattern JCPDS cards 33−0664 and 41−1445, the peaks in Figure 4 marked by pound (#) sign were from the SnO_2 of FTO substrate. Importantly, converted by Bragg diffraction formula, the star (*) sign marked peaks at 2θ values of 26.9, 28.5, and 50.4° of wavelength 1.2398 Å in Figure 4 equaled to 33.6, 35.6, and 63.9° of wavelength 1.54 Å respectively, which was corresponding to the crystal plane of (104), (110) and (300) in pure hexagonal phase of hematite α-Fe_2O_3. Therefore, the FeOOH precursor at 95 °C was completely converted to hematite phase after two steps of high temperature annealing. Of note, the XRD patterns of DHN at 550 and 800 °C were identical with HN's, suggesting that no sodium ions were doped in the hematite nanostructure. Of note, strong (110) diffraction peak indicated these hematite nanostructures are highly oriented in the [110] direction on the substrate, which further suggested the growth axis of these nanostructures should be along [110]. Moreover, the strong (110) diffraction peak of DHN at 800 °C annealing is 2 orders of magnitude higher than 550 °C, which indicated that annealing at 800 °C could intensively increase the crystal orientation along the [110] direction on FTO substrate and maybe strongly enhance the PEC properties of hematite nanostructures because hematite has a strong anisotropic conductivity on this direction.[18,52]

Mössbauer spectra provided detailed structure information for these hematite nanostructures. In detail, The Mössbauer spectra (collected at room temperature) of DHN and HN at 550 and 800 °C were magnetic splitting sextets with broadening line width as shown in Figure 5a, the distribution of hyperfine fields were showed in Figure 5b, and the detailed values of isomeric shift (IS), quadroupole splitting (QS) and magnetic hyperfine field (H_f) were displayed in Table 1. Normally, the broadening line width was attributed to either defects of nanocrystalline[53] or collective magnetic excitation.[54] Since the morphologies of all HN and DHN samples were rather uniform (see Figures 2 and 3), thus the collective magnetic excitation would not produce broadening hyperfine fields[55] and the broadening spectra should be due to the defects of nanocrystalline. Herein, the line width of DHN was broader than the line width of DHN both at 550 and 800 °C, which indicated the lattice defects in DHN was more than in HN both at 550 and 800 °C. The line width of HN and DHN at 550 °C was both broader than at 800 °C, which indicated the annealing step at 800 °C could effectively decrease the lattice defects in hematite nanostructures of HN and DHN. To obtain further information, we resolved the spectra by using a smoothed histogram model.[56] According to the fitting results, four samples have similar IS (isomer shift) and QS (quadrupole
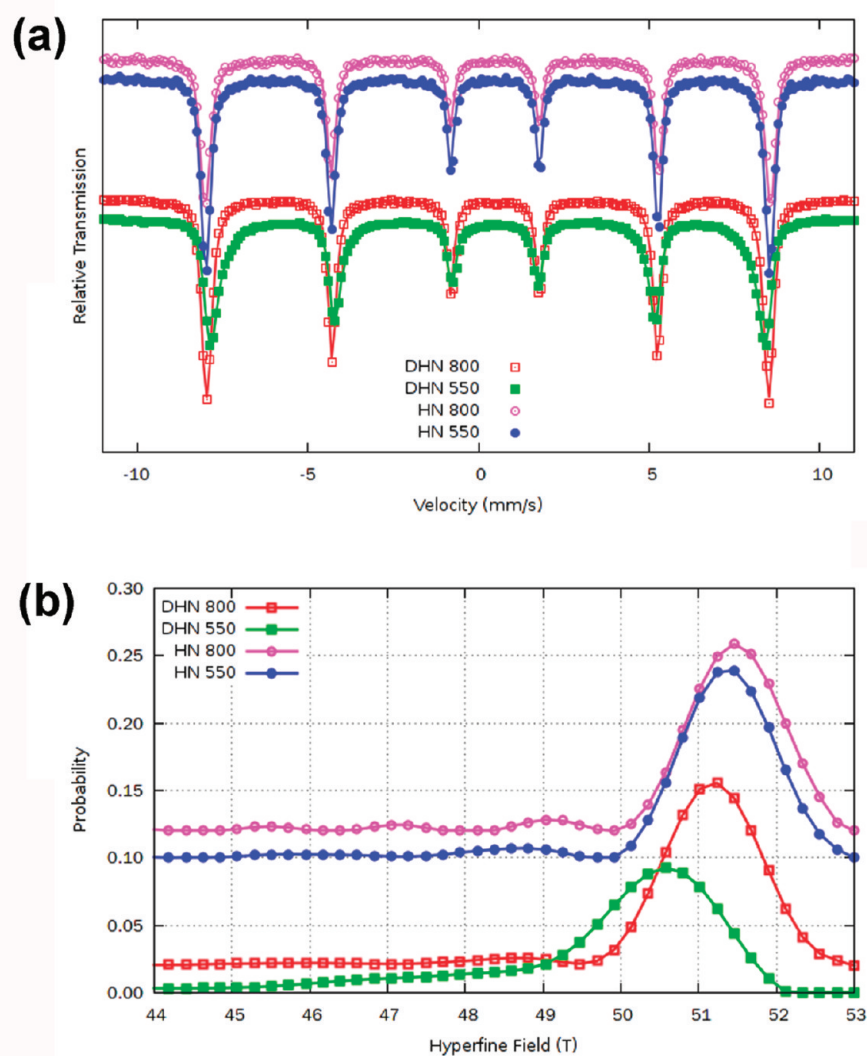
Figure 5. (a) Mössbauer spectra and (b) hyperfine field distribution of HN and DHN of 550 and 800 °C, respectively.

Table 1. Detailed Data from Mossbauer Spectra

	isomer shift (mm/s)	quadroupole splitting (mm/s)	hyperfine field (T)	line wide (mm/s)
HN 550 °C	0.37	−0.21	51.03	0.24
HN 800 °C	0.37	−0.21	51.03	0.21
DHN 550 °C	0.37	−0.21	49.55	0.29
DHN 800 °C	0.37	−0.21	50.87	0.22

split) values of 0.37 and −0.21 mm/s, respectively, which are matched with the reported values of pure hematite.[57] Corresponding to the XRD pattern in Figure 4, the invariable IS and QS value suggested that no other elements or ions were doping in the hematite nanostructures of both HN and DHN. From the hyperfine field distribution as shown in Figure 5b, higher annealing temperature leads to higher average hyperfine field. The most probable hyperfine fields of HN were 51.3 and 51.5 T at 550 and 800 °C, and the most probable hyperfine fields of DHN were 50.4 and 51.2 T for 550 and 800 °C, respectively. The reduced most probable hyperfine fields revealed more lattice defects in the nanocrystalline, which are

confirmed by the XRD patterns in Figure 4. Furthermore, even though the average hyperfine fields of DHN was increased from 49.55 to 50.87 T after annealing at 800 °C, but still weaker than of 51.03 T of HN's, which indicated that considerable amounts of lattice defects were remained in DHN. Therefore, the results of Mössbauer spectra analysis definitely illustrated that except the method of doping elements in semiconductor, the method of adding inorganic salts during the chemical bath deposition step also could introduce defects into the crystal lattice, which was so-called intrinsic defect of semiconductor. In the following in this article, we focused on study the influence of defects in hematite nanostructures on the properties such as light-harvesting, band gap, efficiency of photoelectric conversion and the transport rate of photogenerated carrier.

The photoabsorption behavior of DHN and HN photoanode was characterized by UV−vis spectroscopy. As shown in Figure 6a, the absorption spectra onset between 560 and 650 nm for both DHN and HN were consistent with the 1.9−2.2 eV band gap of hematite and the shoulder peaks at 540 and 430 nm were consistent with the indirect Fe^{3+} d to d and direct O^{2-} p to Fe^{3+} d transitions. Furthermore, DHN exhibited stronger absorption than HN in range of 560−650 nm, while similar absorption with HN in range of 650−750 nm, suggesting that lattice defects in hematite nanostructures offered additional
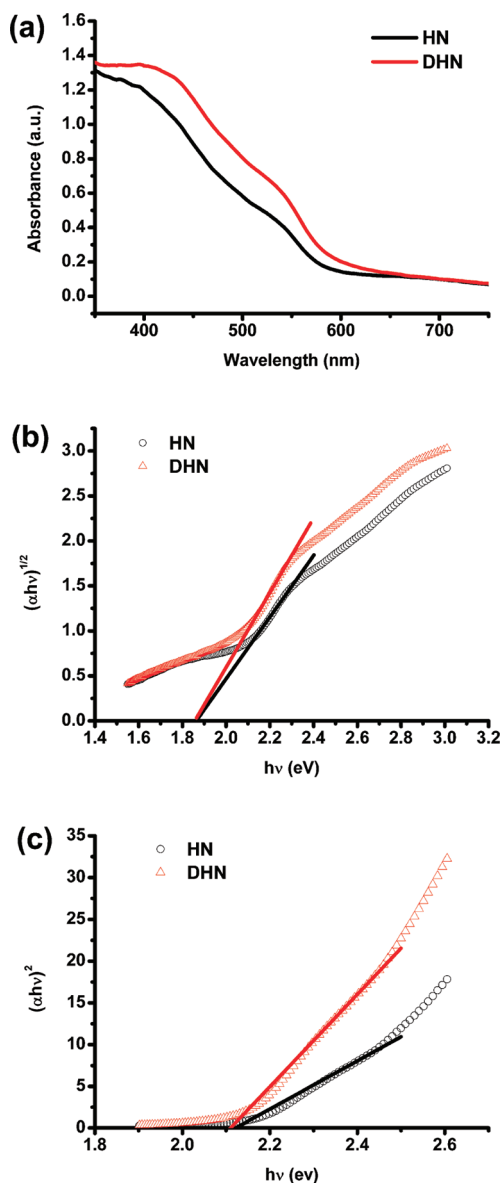
Figure 6. (a) UV−vis spectra of HN and DHN; the optical band gap evaluated by Tauc-plots with the (b) indirect case and (c) direct case. Black and red lines fitted to the linear portion of these plots show the optical band gap approximation.

Figure 7. (a) J−V curves of HN and DHN during illumination and in the dark. (b) IPCE spectra of selected samples, collected at 1.6 V vs RHE. J−V curves were collected with scan rate of 10 mV/s and a scan rage of −0.5−0.8 V (vs AgCl) at room temperature.

Figure 8. Mott−Schottky plots of HN and DHN measured in the dark at a frequency of 1 kHz.

extra optical adsorption in the range of 560−650 nm. This increase in absorption should not come from light scattering effects since there was no absorption increase in the range of 650−750 nm for DHN. In order to estimate the band gaps of DHN and HN, the Tauc-plot curves were drawn from their UV−vis adsorption spectra. Because hematite was a type of indirect semiconductor,[58] the curves of $(\alpha h\nu)^{1/2}$ versus $h\nu$ were plotted according to the following equation[59−61] (shown in Figure 6b)

$$\alpha h\nu = A(h\nu - E_g)^n \tag{4}$$

where α is absorption coefficient, A was the proportional constant, $h\nu$ was the energy of the incident photon and n is 2 for indirect band gap semiconductor. The band gap were estimated through Tauc analysis by a linear fit to the experimental $(\alpha h\nu)^{1/2}$ versus $h\nu$. In this case, the band gap of DHN and HN were both 1.86 eV, which departed the range of
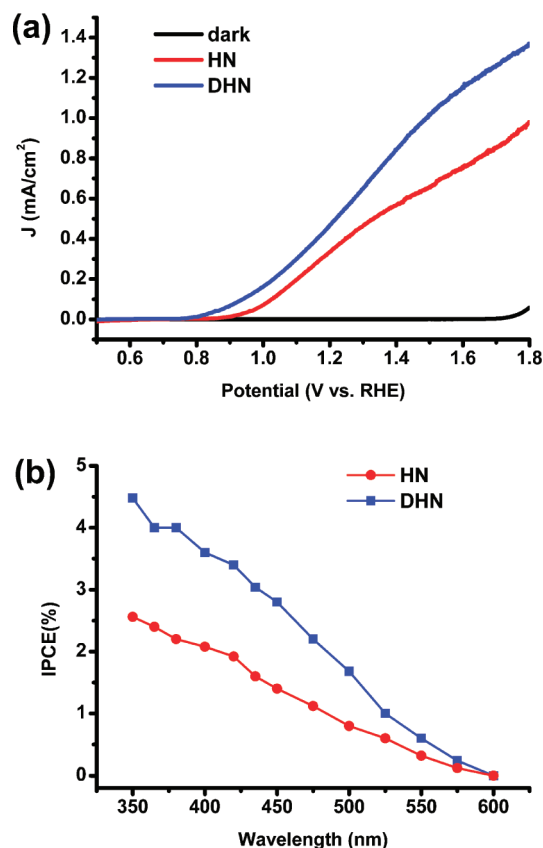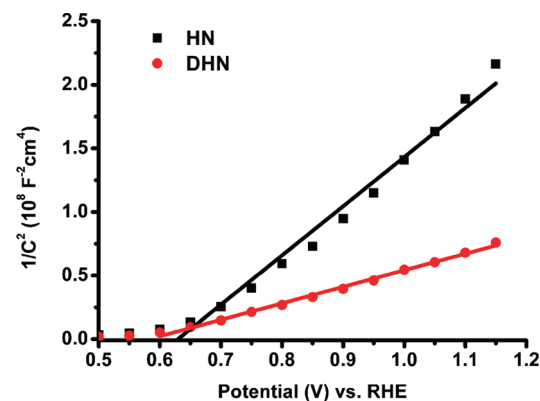
band gap energy (1.9−2.2 eV). However, if the direct transition of $n = 1/2$ was employed (Figure 6c), the best fit was found and 2.1 eV band gap of both DHN and HN was estimated, which indicated that the band gap of hematite were well preserved after introducing the lattice defects in DHN compared with HN.

To study the influence of lattice defects in hematite-nanostructured photoanodes on their PEC performances, we performed photoelectrochemical measurements in an electro-chemical cell of three-electrode configuration at room temperature, with a voltage scan speed of 0.01 V/s in the range from 0.5 to 1.8 V vs RHE. The photocurrent density-applied
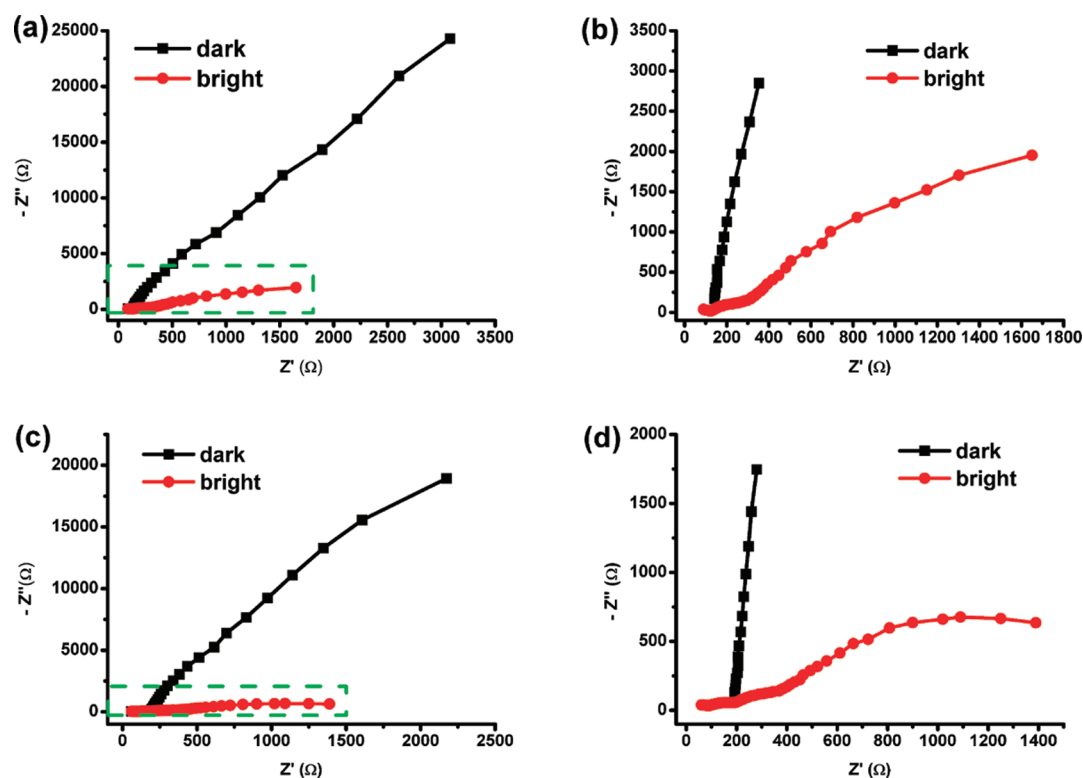
2299

dx.doi.org/10.1021/am300395p | ACS Appl. Mater. Interfaces 2012, 4, 2295−2302

Figure 9. Nyquist plots collected for (a) HN and (c) DHN in the dark and under illumination at 1.6 V vs RHE. (b, d) Magnified views of the region highlighted by the green dashed rectangle in panels a and c.

potential (*J*–*V*) scans of DHN and HN were shown in Figure 7a. Compared with HN, DHN exhibited much higher photocurrent density over the entire potential window. At 1.6 V vs RHE, the photocurrent density of DHN reached 1.2 mA/cm², about twice that of HN. The enhanced photocurrent density for DHN was attributed to the improvement of light-harvesting, which was derived from the introduced lattice defects in hematite nanostructures. Furthermore, the photocurrent onset potential of DHN was at 0.8 V vs RHE, which was lower than the HN's at 0.9 V vs RHE. Therefore, DHN perform more efficient oxygen evolving and improve photocurrent density at the lower bias voltage. To quantitatively investigate the photoactivity of the DHN and HN photoanodes, we collected the incident photon-to-current conversion efficiency (IPCE) data at 1.6 V vs RHE in Figure 7b, which was approximately 1.5 fold higher than HN. Furthermore, the IPCE of DHN was 1–4.5% under different wavelength from 350 to 550 nm irradiations, which was higher than HN's over the entire wavelength. And for the same reason, the higher IPCE value of DHN was also contributed to the presence of lattice defects in hematite nanostructures.

To elucidate the correlation between lattice defects and the enhanced photocurrent and IPCE values, we evaluated capacitances by electrochemical impedance spectroscopy (EIS) measurements. The resultant capacitance values were fit to the Mott–Schottky equation[37]

$$(1/C)^2 = (2/e_0 \varepsilon \varepsilon_0 N_d)(E - E_{FB} - kT/e_0) \quad (5)$$

where *C* was capacitance (F/cm²), e_0 was the electron charge, ε was the hematite dielectric constant of 80,[41,51] ε_0 was the permittivity of vacuum, N_d was the carrier density, *E* was the electrode applied potential, E_{FB} was the flatband potential, *k* was the Boltzmann's constant, and *T* was the temperature.

According to the Mott–Schottky plots in Figure 8, both of the slopes were positive, which indicated that DHN and HN were both n-type semiconductors. Furthermore, calculated by the following equation[45,51]

$$N_d = (2/e_0 \varepsilon \varepsilon_0)[d(1/C^2)/dV]^{-1} \quad (6)$$

Where *V* was voltage, therefore the calculated electron densities of DHN and HN were 1.4×10^{20} cm⁻³ and 4.6×10^{19} cm⁻³, which clearly indicated introducing lattice defects could increase the carrier density in hematite nanomaterials. Moreover, the flatband potential at hematite/electrolyte interface were also estimated by the X-intercepts of the linear region in the Mott–Schottky plots. The 0.58 V vs RHE flatband potential of DHN was more negative than 0.61 V vs RHE of HN, which was in agreement with the onset potential in *J*–*V* plots and therefore was also attributed to the lattice defects in hematite nanostructures.

To investigate the kinetics of the oxidation process at the electrode surface, EIS was carried out. The EIS spectra of DHN and HN under dark and the simulated solar light illumination were presented in Nyquist diagram in Figure 9. The *x* axis represents the real part of the impedance (*Z*′) and the *y* axis represents the imaginary part of the impedance (*Z*″) respectively. Obviously, either HN or DHN in figure 9 showed only one capacitive arc in the dark at 1.6 V vs RHE, suggesting that the Faradaic charge transfer was the limiting step for the oxidation process in the electrode surface. However, under illumination, two capacitive arcs were observed in the Nyquist plot of both HN and DHN, the arc at higher (left) frequencies was correlated to the charge transfer resistance and the lower (right) frequencies was correlated to the mass transfer limitation. The capacitive arcs of both DHN and HN in the bright condition were much smaller than the capacitive arcs in

2300

dx.doi.org/10.1021/am300395p | *ACS Appl. Mater. Interfaces* 2012, 4, 2295–2302

the dark condition, which suggested that the photoexcited carriers increase the conductivity of the hematite nanostructures. Furthermore, the arc size of DHN under illumination was found to be smaller than the HN photoanode under illumination, indicating that the photoexcited carrier transfer resistance in the hematite nanostructures with introduced defects was smaller than in the pure hematite nanostructures.

CONCLUSIONS

We have investigated the influences of lattice defects in nanostructured hematite photoanode on the PEC water splitting performance. In this work, the lattice defects were introduced into the pure nanostructured hematite photoanode via adding inorganic salts during chemical bath deposition in process of photoanode preparation. Importantly, lattice defects introduced in hematite nanostructure decrease the flatband potential from 0.63 to 0.58 V vs RHE, increase the carrier density from 1.83×10^{20} cm^{-3} to 5.44×10^{20} cm^{-3}, reduce the oxygen evolving potential from 0.9 to 0.8 V vs RHE, enhance the light harvest, and enhance the PEC performance 1.5 times higher than the pure nanostructured hematite photoanode at 1.6 V vs RHE. These important features suggest that introducing lattice defects in hematite nanostructures of photoanode may be a promising way to enhance the performance of PEC water splitting for hydrogen preparation.

AUTHOR INFORMATION

Corresponding Author
*E-mail: pengcheng@sinap.ac.cn (C.P.); fchh@sinap.ac.cn (C.F.).

Notes
The authors declare no competing financial interest.

ACKNOWLEDGMENTS

REFERENCES

(1) Turner, J. A. *Science* **1999**, *285*, 687.
(2) Turner, J. A. *Science* **2004**, *305*, 972.
(3) Lewis, N. S. *Nature* **2001**, *414*, 589.
(4) Dunn, S. *Int. J. Hydrogen Energy* **2002**, *27*, 235.
(5) Ogden, J. M. *Ann. Rev. Energy Environ.* **1999**, *24*, 227.
(6) Sivula, K.; Le Formal, F.; Grätzel, M. *ChemSusChem* **2011**, *4*, 432.
(7) Li, Y.; Zhang, J. *Laser Photonics Rev.* **2010**, *4*, 517.
(8) Graetzel, M. *Chem. Lett.* **2005**, *34*, 8.
(9) Fujishima, A.; Honda, K. *Nature* **1972**, *238*, 37.
(10) Bard, K. L. H. a. A. J. *J. Electrochem. Soc.* **1976**, *123*, 1024.
(11) Iwahara, H.; Esaka, T.; Uchida, H.; Maeda, N. *Solid State Ionics* **1981**, *3*, 359.
(12) Wentorf, R.; Hanneman, R. *Science* **1974**, *185*, 311.
(13) Funk, E. J. *Int. J. Hydrogen Energy* **2001**, *26*, 185.
(14) Tseung, A.; Jasem, S. *Electrochim. Acta* **1977**, *22*, 31.
(15) Lindgren, T.; Wang, H.; Beermann, N.; Vayssieres, L.; Hagfeldt, A.; Lindquist, S. E. *Sol. Energy Mater. Sol. Cells* **2002**, *71*, 231.
(16) Saremi-Yarahmadi, S.; Wijayantha, K. G. U.; Tahir, A. A.; Vaidhyanathan, B. *J. Phys. Chem. C* **2009**, *113*, 4768.
(17) Cesar, I.; Kay, A.; Martinez, J. A. G.; Grätzel, M. *J. Am. Chem. Soc.* **2006**, *128*, 4582.
(18) Iordanova, N.; Dupuis, M.; Rosso, K. M. *J. Chem. Phys.* **2005**, *122*, 144305.
(19) Bedja, I.; Hotchandani, S.; Kamat, P. V. *J. Phys. Chem.* **1993**, *97*, 11064.
(20) Bedja, I.; Hotchandani, S.; Carpentier, R.; Vinodgopal, K.; Kamat, P. V. *Thin Solid Films* **1994**, *247*, 195.
(21) Wang, H.; Lindgren, T.; He, J.; Hagfeldt, A.; Lindquist, S. E. *J. Phys. Chem. B* **2000**, *104*, 5686.
(22) Ramana, C.; Utsunomiya, S.; Ewing, R.; Julien, C.; Becker, U. *J. Phys. Chem. B* **2006**, *110*, 10430.
(23) Wolcott, A.; Kuykendall, T. R.; Chen, W.; Chen, S.; Zhang, J. Z. *J. Phys. Chem. B* **2006**, *110*, 25288.
(24) Ahn, K. S.; Yan, Y.; Lee, S. H.; Deutsch, T.; Turner, J.; Tracy, C. E.; Perkins, C. L.; Al-Jassim, M. *J. Electrochem. Soc.* **2007**, *154*, B956.
(25) Ahn, K. S.; Shet, S.; Deutsch, T.; Jiang, C. S.; Yan, Y.; Al-Jassim, M.; Turner, J. *J. Power Sources* **2008**, *176*, 387.
(26) Yan, Y.; Ahn, K. S.; Shet, S.; Deutsch, T.; Huda, M.; Wei, S.; Turner, J.; Al-Jassim, M. *Proc. SPIE* **2007**, *6650*, 66500H.
(27) Yang, X.; Wolcott, A.; Wang, G.; Sobo, A.; Fitzmorris, R. C.; Qian, F.; Zhang, J. Z.; Li, Y. *Nano Lett.* **2009**, *9*, 2331.
(28) Ding, Q. P.; Yuan, Y. P.; Xiong, X.; Li, R. P.; Huang, H. B.; Li, Z. S.; Yu, T.; Zou, Z. G.; Yang, S. G. *J. Phys. Chem. C* **2008**, *112*, 18846.
(29) Khaselev, O.; Turner, J. A. *Science* **1998**, *280*, 425.
(30) Sivula, K.; Zboril, R.; Le Formal, F.; Robert, R.; Weidenkaff, A.; Tucek, J.; Frydrych, J.; Grätzel, M. *J. Am. Chem. Soc.* **2010**, *132*, 7436.
(31) Cherepy, N. J.; Liston, D. B.; Lovejoy, J. A.; Deng, H.; Zhang, J. Z. *J. Phys. Chem. B* **1998**, *102*, 770.
(32) Brillet, J.; Grätzel, M.; Sivula, K. *Nano Lett.* **2010**.
(33) Mohapatra, S. K.; John, S. E.; Banerjee, S.; Misra, M. *Chem. Mater.* **2009**, *21*, 3048.
(34) Beermann, N.; Vayssieres, L.; Lindquist, S. E.; Hagfeldt, A. *J. Electrochem. Soc.* **2000**, *147*, 2456.
(35) Wang, H.; Deutsch, T.; Turner, J. A. *J. Electrochem. Soc.* **2008**, *155*, F91.
(36) Hong, Y. R.; Liu, Z.; Al-Bukhari, S. F. B. S. A.; Lee, C. J. J.; Yung, D. L.; Chi, D.; Hor, T. S. A. *Chem. Commun.* **2011**, *47*, 10653.
(37) Hahn, N. T.; Mullins, C. B. *Chem. Mater.* **2010**, *22*, 6474.
(38) Glasscock, J. A.; Barnes, P. R. F.; Plumb, I. C.; Savvides, N. *J. Phys. Chem. C* **2007**, *111*, 16477.
(39) Satsangi, V. R.; Kumari, S.; Singh, A. P.; Shrivastav, R.; Dass, S. *Int. J. Hydrogen Energy* **2008**, *33*, 312.
(40) Sartoretti, C. J.; Alexander, B. D.; Solarska, R.; Rutkowska, I. A.; Augustynski, J.; Cerny, R. *J. Phys. Chem. B* **2005**, *109*, 13685.
(41) Cesar, I.; Sivula, K.; Kay, A.; Zboril, R.; Grätzel, M. *J. Phys. Chem. C* **2008**, *113*, 772.
(42) Jang, J. S.; Lee, J.; Ye, H.; Fan, F. R. F.; Bard, A. J. *J. Phys. Chem. C* **2009**, *113*, 6719.
(43) Kleiman-Shwarsctein, A.; Hu, Y. S.; Forman, A. J.; Stucky, G. D.; McFarland, E. W. *J. Phys. Chem. C* **2008**, *112*, 15900.
(44) Gaudon, M.; Pailhe, N.; Majimel, J.; Wattiaux, A.; Abel, J.; Demourgues, A. *J. Solid State Chem.* **2010**, *183*, 2101.
(45) Ling, Y.; Wang, G.; Wheeler, D. A.; Zhang, J. Z.; Li, Y. *Nano Lett.* **2011**, *11*, 2119.
(46) Hu, Y. S.; Kleiman-Shwarsctein, A.; Forman, A. J.; Hazen, D.; Park, J. N.; McFarland, E. W. *Chem. Mater.* **2008**, *20*, 3803.
(47) Thimsen, E.; Le Formal, F.; Grätzel, M.; Warren, S. C. *Nano Lett.* **2011**, *11*, 35.
(48) Gonçalves, R. H.; Lima, B. H. R.; Leite, E. R. *J. Am. Chem. Soc.* **2011**, *133*, 6012.
(49) Vayssieres, L.; Beermann, N.; Lindquist, S. E.; Hagfeldt, A. *Chem. Mater.* **2001**, *13*, 233.
(50) Klencsár, Z.; Kuzmann, E.; Vértes, A. *J. Radioanal. Nucl. Chem.* **1996**, *210*, 105.
(51) Wang, G.; Ling, Y.; Wheeler, D. A.; George, K. E. N.; Horsley, K.; Heske, C.; Zhang, J. Z.; Li, Y. *Nano Lett.* **2011**, *11*, 3503.
(52) Kay, A.; Cesar, I.; Grätzel, M. *J. Am. Chem. Soc.* **2006**, *128*, 15714.
(53) Van der Kraan, A. *Phys. Status Solidi A* **1973**, *18*, 215.
(54) Topsoe, H.; Dumesic, J. *Applications of Mossbauer Spectroscopy*; Academic Press: New York, 1980; Vol. 2, p 55.

(55) Jiang, J. S.; Yang, X. L.; Chen, L. W.; Zhou, N. F. *Appl. Phys. A: Mater. Sci. Process* **1988**, *45*, 245.

(56) Hesse, J.; Rubartsch, A. *J. Phys. E* **1974**, *7*, 526.

(57) Sanchez, L.; Arboleda, J.; Saragovi, C.; Zysler, R.; Barrero, C. *Physica B* **2007**, *389*, 145.

(58) Kennedy, J. H.; Frese, K. W., Jr *J. Electrochem. Soc.* **1978**, *125*, 709.

(59) Tauc, J.; Menth, A. *J. Non-Cryst. Solids* **1972**, *8*, 569.

(60) Wang, Y.; Thomas, P. J.; O'Brien, P. *J. Phys. Chem. B* **2006**, *110*, 21412.

(61) Pradhan, D.; Leung, K. T. *Langmuir* **2008**, *24*, 9707.